

Effect of Sn Loading on the Characteristics of Pt Electrocatalysts Supported on Reduced Graphene Oxide for Application as Direct Ethanol Fuel Cell Anode

Guilherme L. Cordeiro^{1,*}, Valter Ussui¹, Nildemar A. Messias¹, Ricardo M. Piasentin², Nelson B. de Lima¹, Almir O. Neto², Dolores R. R. Lazar¹

¹ Materials Science and Technology Center, Energy and Nuclear Research Institute, National Nuclear Energy Commission (IPEN-CNEN/SP), Lineu Prestes Avenue, 2242 – Zip Code: 05508-000 – São Paulo, Brazil

² Fuel Cells and Hydrogen Center, Energy and Nuclear Research Institute, National Nuclear Energy Commission (IPEN-CNEN/SP), Lineu Prestes Avenue, 2242 – Zip Code: 05508-000 – São Paulo, Brazil

*E-mail: gcordeiro@usp.br

Received: 15 February 2017 / Accepted: 4 March 2017 / Published: 12 April 2017

The effect of Sn loading (5–30 mol %) on Pt catalysts supported on reduced graphene oxide was investigated for ethanol electro-oxidation in acidic medium. Reduced graphene oxide was synthesized via graphite oxidation–exfoliation process in liquid phase and chemical reduction. Pt and Pt_xSn_y catalysts were deposited on reduced graphene oxide by a NaBH₄ impregnation–reduction method. The adopted procedures allowed the synthesis of graphene-like nanosheets where single Sn-doped Pt nanoparticles were impregnated. Pt lattice parameter and micro-strain increased with Sn addition, confirming the formation of a solid solution. Concerning ethanol electro-oxidation, Pt was more active when supported on reduced graphene oxide whereas the introduction of Sn enhanced the catalyst activity, leading to lower ethanol oxidation potentials and higher current densities.

Keywords: reduced graphene oxide, platinum, tin, ethanol electro-oxidation

1. INTRODUCTION

The last decade's environmental consensus has been driving the adoption of policies intended to boost investment in emerging technologies. Fuel cells have been proven to represent efficient and clean energy conversion systems. Future possibilities of application are identified along with auxiliary power units and transportation [1]. Specifically, development of direct ethanol fuel cells (DEFCs) will open potential strategies mainly for countries where economy is based on agriculture. Brazil, for example, has the world's most successful biofuel program, which comprises ethanol production from

sugar cane fermentation. Furthermore, ethanol is an attractive fuel because of its low toxicity and high energy density [2]. Although DEFCs represent an attractive choice for sustainable energy conversion, ethanol cannot be fully electro-oxidized at low temperatures (60 – 120 °C) due to the difficulty of breaking C–C bond. This major challenge has imposed the use of Pt catalysts for electrode reactions. Pt has been widely studied in ethanol oxidation reaction (EOR) because of the highest activity, chemical stability, high exchange current density and superior work function [3,4].

Nevertheless, the high cost of Pt limits DEFCs' commercialization. In order to decrease the content of Pt without activity loss, binary combinations have been widely studied in EOR. The contribution of alloying has resulted in an enhancement of the electrocatalytic activity of Pt through the combined bifunctional and electronic effects. Precisely, a bifunctional effect has been associated to the presence of phases that aid in the dissociation of water to form surface hydroxides, which can readily oxidize adsorbed intermediate byproducts from EOR. Electronic effect has been related to an improved reactive surface as a consequence of the changes in Pt valence electronic structure. Up to now, the most extensively investigated bimetallic catalysts have been PtRu [5,6] and PtSn [7,8]. These binary combinations have been regarded as some of the most efficient for EOR according to the bifunctional effect. In terms of electronic effect, it has been proposed that a facile EOR can be achieved with PtSn catalysts operating in acidic medium [9,10].

Further enhancement in the electrocatalytic activity of Pt and Pt-based catalysts has been associated to the support, which requires large surface area and high conductivity. Recently, graphene has been investigated as an electrocatalyst support because of its high surface area (theoretical value of $2630 \text{ m}^2 \cdot \text{g}^{-1}$ for a single layer) and high charge-carrier mobility ($2000\text{--}5000 \text{ cm}^2 \cdot \text{V}^{-1} \cdot \text{s}^{-1}$) [11,12]. Kakei [13] investigated the electrochemical characteristics of graphene oxide-supported Pt₃Sn electrocatalyst for ethanol oxidation. High current densities, lower oxidation potential and higher efficiency were obtained with respect to graphene oxide-supported Pt. Very recently, Qu et al. [14] obtained Pt/SnO₂/graphene composites with superior electrocatalytic activity and stability for EOR as compared with the commercial Pt/C catalyst. The unique properties of Pt/SnO₂/graphene were attributed to the close-connected structure between Pt and SnO₂ nanoparticles and the strong metal–support interaction. Despite of good electro-oxidation properties, one of the main issues concerning the use of graphene has been related to the development and scale-up of an efficient and inexpensive mass-production method for obtaining ultrathin films with less degraded electronic mobility [12,15].

Among the various methods of synthesis, liquid-phase oxidation of graphite [16-19] has been reported as the most cost effective strategy for obtaining multi-, few- and single-layer chemically converted graphene (CCG), terminology that includes graphene oxide (GO) and reduced graphene oxide (rGO) [20]. The most commonly used method for the synthesis of CCG was developed by Hummers and Offeman [18]. In Hummers' procedure, graphite is oxidized by treatment with KMnO₄ and NaNO₃ in concentrated H₂SO₄, whereas exfoliation is achieved by sonication of graphite oxide in water, followed by centrifugation. Despite its high efficiency, Hummers' method leads to generation of toxic gases, such as NO₂ and N₂O₄. In order to eliminate the formation of hazardous products and to improve safety, Marcano et al. [19] replaced NaNO₃ by H₃PO₄. Chemical conversion of the nonconductive hydrophilic graphene oxide to a conductive graphitic material has been achieved by

using a wide range of reducing agents [21]. One of these, L-ascorbic acid, also known as vitamin C, has been used as a primary reducing agent because of its environmentally safe feature [21-24].

Hence, the aim of the present work was to study the effect of Sn addition in the electrocatalytic activity of Pt/rGO catalysts for EOR. Membrane/electrodes assemblies (MEAs) were also manufactured and the electric characteristics of single DEFCs were determined in order to establish a correlation between materials' properties and electroactivity. In particular, this work also focused on single fuel cell tests, which are a prerequisite for prediction of the performance of large-scale fuel cell electrodes on the basis of electrochemical studies. Therefore, contribution of the present work is extended to the investigation of electrocatalytic activity under cell relevant conditions (e.g., continuous reactant flow, steady-state, temperature).

2. MATERIALS AND METHODS

2.1. Synthesis of graphene oxide and reduced graphene oxide

The oxidation-exfoliation of graphite (100 mesh flakes, Aldrich) was adapted from an improved Hummers' method [19]. Typically, 1.0 wt % graphite flakes was added to a 9:1 (v/v) mixture of concentrated H₂SO₄ (95-98 % Synth) and H₃PO₄ (85 % Synth) followed by addition of 6.0 wt % KMnO₄ (99 % Aldrich) under stirring. Maintaining the stirring, the suspension was heated to 45 °C in a water-bath for 8 h. The suspension was naturally cooled to room temperature for 16 h followed by slow addition of 30 mL of hydrogen peroxide (29-32 % Synth) in an ice-bath in order to suppress graphite oxidation [25].

The mixture was centrifuged (Fanem Excelsa® 3) at 2000 rpm for 1 h and the supernatant was decanted away. The remaining solid material was washed with deionized water by an association of sonication (Unique USC-2800, ultrasound frequency: 40 kHz, nominal power: 154 W) and centrifugation procedures until the supernatant pH reached 2–3. The material remaining after this sonication-centrifugation process was coagulated with deionized water, and the resulting suspension (1.5 g·L⁻¹) was ultrasonically treated for an extra 1 h before storage. For synthesized graphene oxide characterization, an aliquot of this slurry was collected, filtered, washed with a 1.0 mol·L⁻¹ methanol (99.8 % Merck) solution to neutral pH, dried overnight at air and deagglomerated in an agate mortar.

The reduction procedure was performed by addition of 1.5 g L-ascorbic acid (99.7 % Merck), under stirring, into 100 mL GO suspension after adjusting the pH at 6–7 with 1.0 mol·L⁻¹ ammonium hydroxide (28-30 %) solution. The mixture was heated at 95 °C and the reaction was maintained for 1 h followed by cooling to room temperature [24]. The obtained black suspension was centrifuged at 2000 rpm for 30 min and the supernatant was easily decanted away due to the great tendency of rGO to flocculate in aqueous medium. Resultant reduced graphene oxide was poured onto a 1.0 mol·L⁻¹ hydrochloric acid (37 % Synth) solution, followed by 10 min sonication in an ultrasonic bath and centrifugation for 30 min. The slurry was washed with deionized water and centrifuged. The latter process was repeated until neutral pH. Finally, the remaining solid was poured onto a 1.0 mol·L⁻¹

methanol solution, sonicated and centrifuged. Obtained powders were oven-dried at 60 °C for 16 h and deagglomerated.

2.2. Synthesis of Pt and Pt_xSn_y electrocatalysts supported on reduced graphene oxide

For the synthesis of 20 wt% Pt supported on reduced graphene oxide, 2.1 mL of H₂PtCl₆·6H₂O (19.05 mg·mL⁻¹ Aldrich) solution was added into 50 mL of a 6.5 mol·L⁻¹ isopropyl alcohol (99.5 % Alphatec) solution under stirring. Subsequently, 160 mg of synthesized rGO powder was dispersed in the solution followed by 10 min sonication in a probe (Unique DES500, ultrasound frequency: 20 kHz, power: 100 W). Then, 10 mL of a 0.01 mol·L⁻¹ NaOH solution containing NaBH₄ (molar ratio NaBH₄/metals fixed at 5:1) was rapidly poured into the electrocatalyst precursor solution. For the evaluation of the effect of Sn addition on the characteristics of Pt electrocatalyst, all preparation procedures were similar to the experiments described above, except for the addition of a determined SnCl₂·2H₂O (99.99 % Synth) amount before the step of rGO powder dispersion. Metals content was fixed at 20 wt % and Sn loading was varied from 5 to 30 mol %.

At the end of impregnation–reduction reactions, the slurries reached pH 3.0. Resultant suspensions from all set of experiments were aged for 30 min under stirring, vacuum-filtrated, washed with deionized water, dried in an oven at 70 °C for 2 h and deagglomerated in an agate mortar. Sn-containing samples were designated as Pt_xSn_y, where *x* and *y* correspond to Pt and Sn molar composition, respectively.

2.3. Samples physical and chemical characterization

The crystalline structures of precursor graphite, synthesized graphene oxide (GO), reduced graphene oxide (rGO), and rGO-supported electrocatalysts were investigated by X-ray diffraction (Rigaku, Multiflex) with Cu-K α radiation. For graphite, GO and rGO, analysis conditions were set at a 2 θ range 5–50°, step size 1° and counting time of 1 min. Supported electrocatalysts were characterized using a 2 θ range 10–90°, step size 0.02° and counting time of 10 s. For phase identification, the obtained data were compared to ICDD (International Center for Diffraction Data) cards. In order to evaluate the effect of Sn addition in catalyst structure, Pt lattice parameter was determined by Rietveld analysis while mean crystallite size and micro-strain were determined by Williamson-Hall (W-H) analysis.

Chemical and structural changes during reduced graphene oxide synthesis were investigated by means of diffuse reflectance infrared Fourier transform spectroscopy (Thermo Nicolet Nexus 670 FTIR). Measurements were carried out in transmittance mode with a KBr pellet method at a wavenumber range 4000–400 cm⁻¹.

Additional information about the structure of the as-synthesized reduced graphene oxide powder was obtained by Raman spectroscopy (Renishaw inVia Raman Microscope). Raman spectra were acquired using a 532 nm excitation laser. To concentrate the laser beam at the sample, a 50x magnification objective lens with numerical aperture of 0.75 was placed above. The incident laser

power was carefully tuned to avoid sample damage and, therefore, measurements were performed with 1% of total power. All measurements were run in triplicate, thus the presented spectrum represents a mean of the data.

Tin content in synthesized electrocatalysts was determined by X-ray microanalysis (JCM-6000, JEOL) and the microstructure of the support and supported electrocatalysts was examined by means of transmission electron microscopy (JEM-2100, JEOL). The particle size distributions of electrocatalysts were determined by counting 200 to 300 particles from a set of five images with the aid of Lince Image Analyser. Measure of the size was defined by the maximum dimension of each particle in any direction.

2.4. Electrochemical measurements

Cyclic voltammetry and chronoamperometry experiments were performed with a home-made three-electrode cell with a Pt plate (2 cm²) as counter electrode, a reversible hydrogen electrode (RHE) as the reference electrode and a glassy carbon electrode (0.196 cm²) as the working electrode. The latter was modified with the synthesized catalysts (Pt/rGO, Pt_{0.95}Sn_{0.05}/rGO, Pt_{0.85}Sn_{0.15}/rGO and Pt_{0.75}Sn_{0.25}/rGO) by an ultrathin coating technique [26]. For the preparation of the modified working electrode, 6 mg of the electrocatalyst powder were mixed with 1 mL of deionized water, 100 μL of isopropyl alcohol and 40 μL of Nafion solution (5 wt %, DuPont). The suspension was treated in an ultrasound bath for 30 min and 10 μL were coated on the glassy carbon surface with a pipette followed by drying at 70 °C for 15 min. Prior to each electrochemical characterization, 45 mL of a 0.5 mol·L⁻¹ H₂SO₄ solution were saturated with N₂ for 45 min. After immersion of the electrodes in the solution, electrochemical tests were carried out at room temperature with a potentiostat/galvanostat (PGSTAT30, Autolab). Cyclic voltammograms were firstly recorded in 0.5 mol·L⁻¹ H₂SO₄ solution followed by the addition of 2.7 mL of ethanol (99.5 % Alphatec) into the system with the aim of obtaining voltammetric curves in 0.5 mol·L⁻¹ H₂SO₄/1.0 mol·L⁻¹ C₂H₅OH. Cyclic voltammetry experiments were conducted in the range 0.05–0.80 V at a scan rate of 10 mV·s⁻¹. Chronoamperometric curves were registered at 0.5 V in 0.5 mol·L⁻¹ H₂SO₄/1.0 mol·L⁻¹ C₂H₅OH for 30 min. For comparison purposes, the working electrode was also coated with a commercially available Pt reference catalyst (20 wt % Pt/Vulcan XC-72, BASF) and tested. Electrochemical measurements were run in duplicate and, therefore, presented results represent a mean of the data.

2.5. MEAs fabrication and tests in DEFCs

Anode and cathode electrodes were manufactured by brush-painting catalyst inks on 5 cm² carbon papers. For anodes preparation, an amount of the rGO-supported Pt, rGO-supported Pt_xSn_y and a commercially available Pt reference catalyst (20 wt % Pt/Vulcan XC-72, BASF) were used in order to obtain a Pt loading of 1.0 mg·cm⁻². Then, each catalyst mass was dispersed in a known volume of Nafion (5 wt%, DuPont) solution to yield a suspension containing 35 wt % Nafion, followed by ultrasonic treatment for 30 min and drying at 70 °C. In sequence, powders were deagglomerated and

re-dispersed in 1.0 mL of a $6.5 \text{ mol}\cdot\text{L}^{-1}$ isopropyl alcohol solution to obtain catalyst inks. Cathodes were similarly prepared, except for using carbon-supported 20 wt% Pt (BASF) as the catalyst source. Commercial Nafion 117 membrane was immersed in warm deionized water ($80 \text{ }^\circ\text{C}$) and treated with 3% H_2O_2 and $1.0 \text{ mol}\cdot\text{L}^{-1}$ H_2SO_4 to exchange Na^+ in the membrane with H^+ [13]. All MEAs were fabricated by hot pressing anode/Nafion membrane/cathode under a pressure of $225 \text{ kgf}\cdot\text{cm}^{-2}$ at $125 \text{ }^\circ\text{C}$ for 6 min. Single DEFCs tests were carried out at $100 \text{ }^\circ\text{C}$. Ethanol ($2.0 \text{ mol}\cdot\text{L}^{-1}$) was fed in the anode at $1.0 \text{ mL}\cdot\text{min}^{-1}$ under 1.0 bar pressure and pure humidified oxygen was fed in the cathode at 200 sccm under 2.0 bar pressure. Before each test, the cell was simultaneously fed with ethanol and oxygen at the operating temperature for 5,000 s to achieve stabilization. Three polarization curves (i vs. E) were obtained every 15 min by a galvanostatic method in which an applied current was varied at steps of 0.1 A. Power densities were also calculated and the results presented as i vs. P curves. All fuel cell tests were run in triplicate and the results represent a mean of the data.

3. RESULTS AND DISCUSSION

3.1. Physical and chemical characterization of graphene oxide and reduced graphene oxide

X-ray diffraction patterns of the starting graphite (G), synthesized graphene oxide (GO) and reduced graphene oxide (rGO) are presented in Fig. 1. Graphite has an intense peak at 26.3° corresponding to the (002) plane, as indicated by comparison of diffraction data and ICDD card 25-0284. On the conversion to graphene oxide (GO), this peak gradually shifts to a lower angle ($2\theta = 9.1^\circ$). This structural change occurs as a result of an expansion of the graphitic lamellas due to a chemical functionalization caused by the oxidation process [27-29]. Moreover, broadening of (002) peak indicates a low degree of crystallinity. This behavior may be explained by the introduction of defects in sp^2 carbon hexagonal networks during graphite oxidation, as suggested by Hu et al [30].

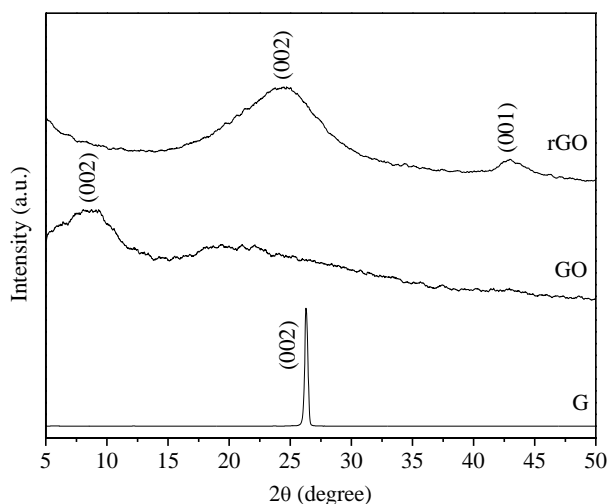


Figure 1. Normalized X-ray diffraction patterns of the starting graphite (G), synthesized graphene oxide (GO) and reduced graphene oxide (rGO).

In relation to GO (Fig. 1), X-ray diffraction analysis also revealed the presence of a wide peak between 15 and 35°, which is not considered as a characteristic peak of graphene oxide. This peak might be related to the formation of reduced graphene oxide since methanol has shown a reducing capability towards GO [31], demonstrating the influence of the washing step with a 1.0 mol·L⁻¹ methanol solution on graphene oxide functionalization. After reduction of GO (Fig. 1), the (002) plane shifted towards a higher angle value ($2\theta = 24.5^\circ$) due to removal of some oxygen functional groups. This shift has been attributed to a partial restoration of the graphitic structure, which can be achieved by chemical reduction [22-24,32]. X-ray analysis also revealed the presence of a peak at 42.5°, which is another characteristic peak of rGO [32].

Removal of some functional oxygen groups attached to graphene oxide during reduction step was investigated by diffuse reflectance infrared Fourier transform spectroscopy (DRIFTS), as presented in Fig. 2. Graphene oxide DRIFTS spectrum illustrates the presence of a broad band centered at 3423 cm⁻¹, corresponding to stretching vibrations of bonded O–H and adsorbed water molecules. The low-intensity doublet bands at 2966 and 2923 cm⁻¹ were assigned to the *sp*³-hybridized C–H asymmetric and symmetric stretching vibrations, respectively. Bands in the region 2400–2000 cm⁻¹ might be associated to stretching vibrations of S–H and/or P–H. A weak absorption band at 1716 cm⁻¹ was assigned to O–H vibrations of carboxylic groups.

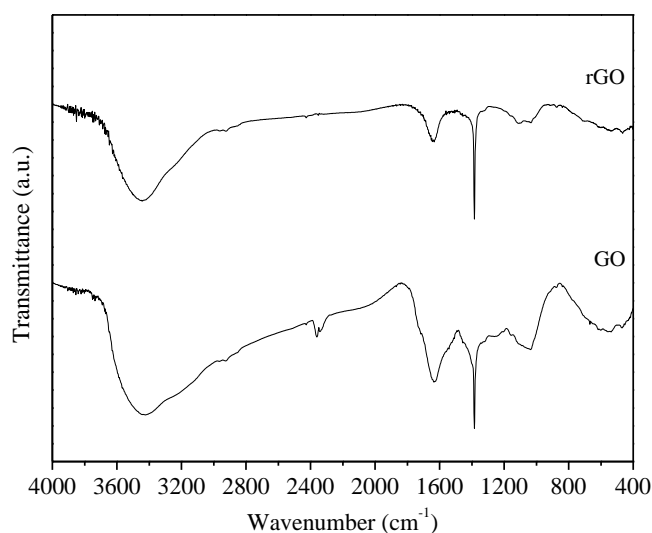


Figure 2. Normalized DRIFTS spectra of the synthesized graphene oxide (GO) and reduced graphene oxide (rGO).

A medium absorption centered at 1637 cm⁻¹ was interpreted to be a C=O stretching vibration of a carbonyl group, whereas the sharp peak at 1384 cm⁻¹ corresponded to a C–H bending vibration of a methyl (–CH₃) or methylene (–CH₂–) group. The presence of absorption bands related to C–H groups might be an indication of a disruption of the *sp*² structure, which was possibly caused by hydrogenation of the hexagonal lattice during oxidation step [15,30]. This feature is in agreement with the broadening of the (002) diffraction peak, as shown in Fig. 1. Therefore, the low degree of crystallinity might be associated to the modification of the regular array of carbon atoms due to

formation of a partially hydrogenated structure. Assignment of the band at 1025 cm^{-1} might be related to C–O stretching vibration of an epoxy group, while the band in the range $900\text{--}400\text{ cm}^{-1}$ is likely to correspond to =C–H out-of-plane bending vibrations in aromatic rings [24,31,32].

After reducing GO, the intensities of the DRIFTS bands (Fig. 2) corresponding to oxygen functionalities, such as O–H, C=O and C–O vibrations, decreased considerably as shown by the reduced graphene oxide DRIFTS spectrum, which confirmed that most of oxygen functional groups were removed. The reduction efficiency of GO suspensions by L-ascorbic acid has been demonstrated by several studies [22–24] and the proposed reaction mechanism proceeded via L-ascorbic acid dissociation to anions with capability of promoting nucleophilic attacks on GO oxygen functional groups [21]. In contrast, a change in the intensities of bands located at 1384 and $900\text{--}400\text{ cm}^{-1}$, compared to the respective intensities in GO spectrum, suggests that the reduction process is not sufficient for completely restoration of carbon sp^2 hybridization.

The presence of lattice distortions was also confirmed by Raman spectroscopy. The band centered around 1357 cm^{-1} , commonly named as D band, has been related to atomic defects within the layers, as suggested by X-ray diffraction (Fig. 1) and infrared (Fig. 2) results.

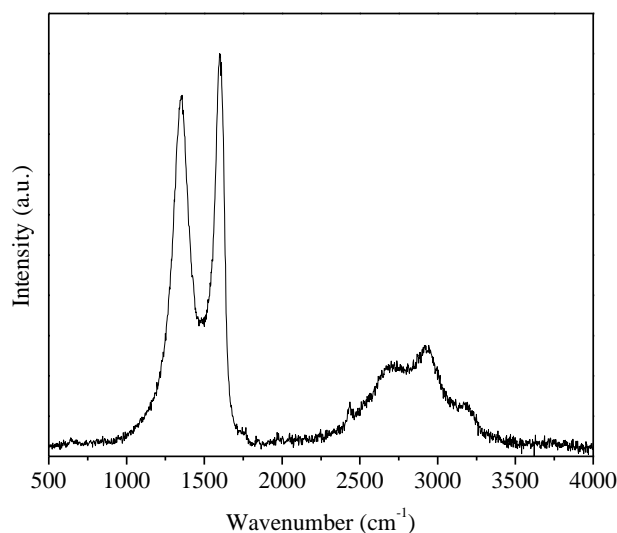


Figure 3. Normalized Raman spectrum of reduced graphene oxide (rGO) recorded using a 532 nm excitation laser with 1% of total power.

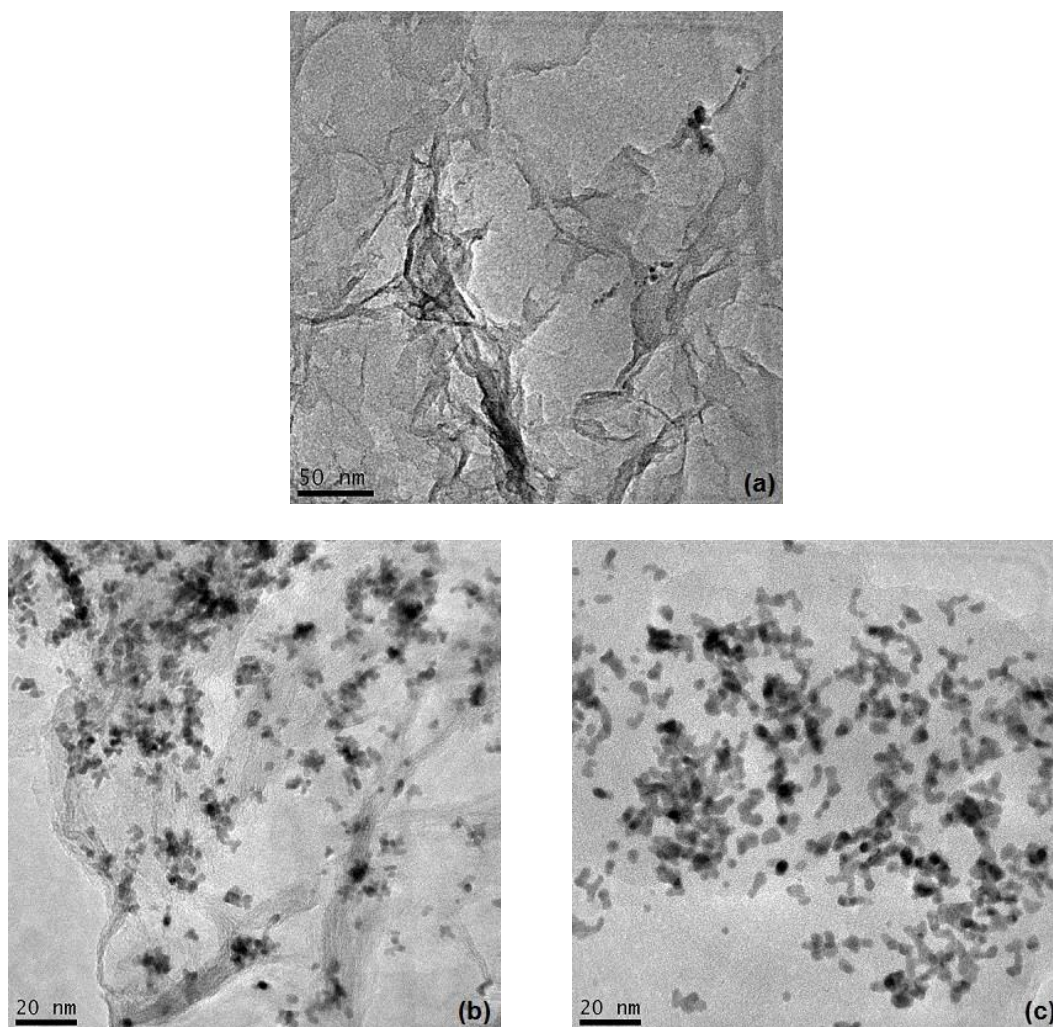
Moreover, the synthesized reduced graphene oxide is not constituted by a single layer of carbon atoms considering three observed features: (1) the shift of the G band to higher wavenumbers (around 1610 cm^{-1}), (2) the relation between the intensities of G and G' bands and the (3) broadening of G' band ($2500\text{--}2800\text{ cm}^{-1}$) [33,34]. Furthermore, the relative intensities of D to G bands have been used in the evaluation of the amount of defects in the sample. In comparison to a similar study carried out by Hu et al. [30], the ratio calculated from the spectrum in Fig. 3 ($I_D/I_G = 0.89$) is indicative of a minor defect concentration in the synthesized reduced graphene oxide.

A representative transmission electron microscopy image of rGO is shown in Fig. 4(a). Overall, reduced graphene oxide consisted of a fragmented thin film. This feature might be a result of an excessive centrifugation and ultrasonic treatment used along washing and exfoliation steps [24].

3.2. Physical and chemical characterization of Pt and Pt_xSn_y electrocatalysts supported on reduced graphene oxide

The microstructure of Pt/rGO and Pt_xSn_y/rGO electrocatalysts was investigated by transmission electron microscopy. All samples consisted of agglomerated and round-shaped nanoparticles over (almost) transparent graphene-like films as presented in Fig. 4(b–e). In general, the particle size slightly varied with Sn content. Diameter distributions of the nanoparticles (Fig. 5) were estimated from TEM images and the results suggested a similar trend after the addition of Sn.

X-ray diffraction patterns of synthesized electrocatalysts are presented in Fig. 6. According to the diffractograms, X-ray analysis only revealed the presence of metallic Pt, in accordance with ICDD card number 76-414, apart from the support phase. SnO₂ was not identified for powders with Sn loading varying from 5 to 30 mol %. Furthermore, broadening of Pt X-ray diffraction peaks could not be observed after Sn addition, although Sn was detected by microanalysis (Table 1).



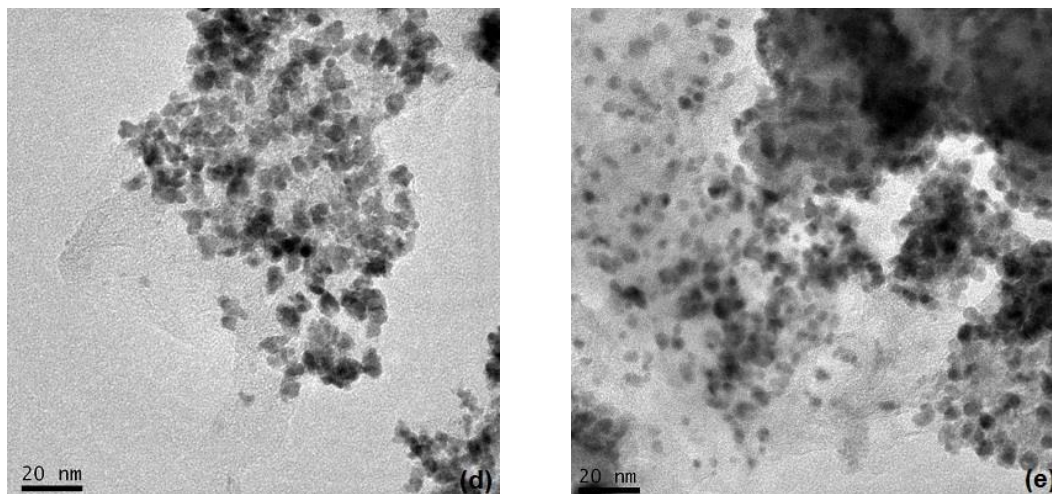


Figure 4. Transmission electron microscopy (TEM) images of reduced graphene oxide (a), and metals supported on reduced graphene oxide: Pt (b), Pt_{0.95}Sn_{0.05} (c), Pt_{0.85}Sn_{0.15} (d), Pt_{0.75}Sn_{0.25} (e).

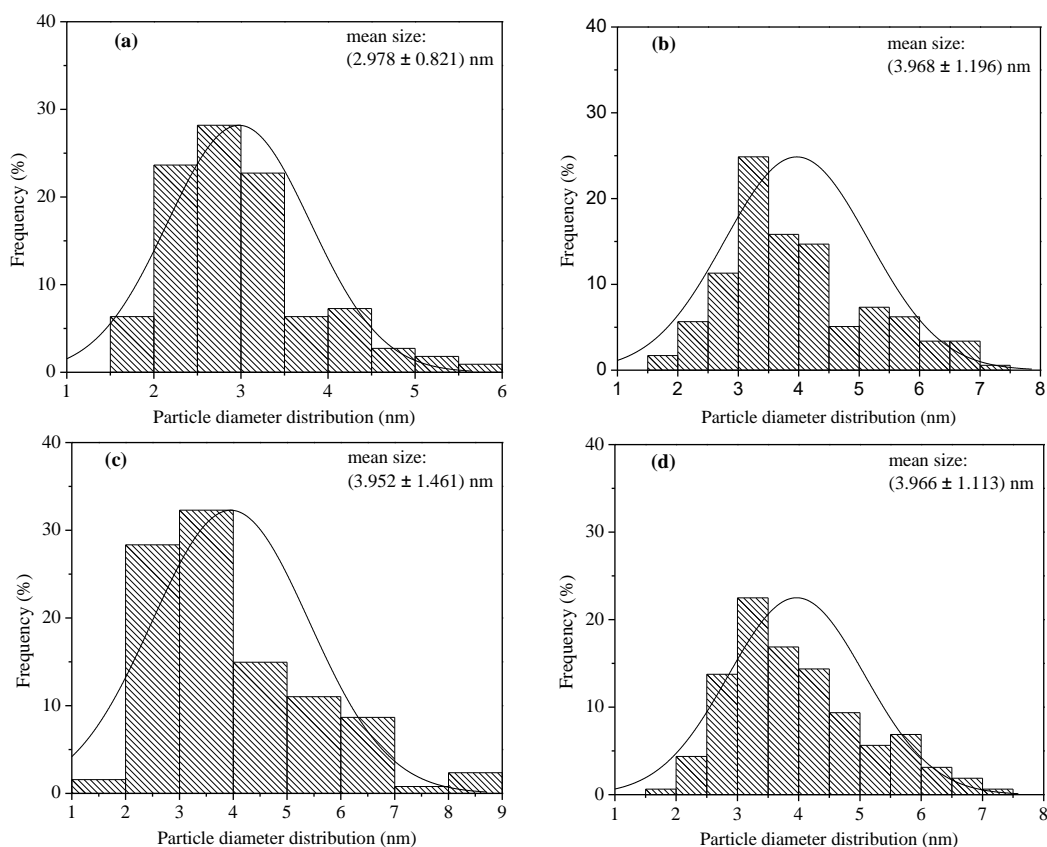


Figure 5. Diameter distributions of Pt (a), Pt_{0.95}Sn_{0.05} (b), Pt_{0.85}Sn_{0.15} (c) and Pt_{0.75}Sn_{0.25} (d) nanoparticles dispersed on the surface of reduced graphene oxide.

A close examination of X-ray patterns by means of structural refinement with Rietveld method revealed an increase in Pt lattice parameter with Sn addition (Table 1), suggesting the formation of a solid solution.

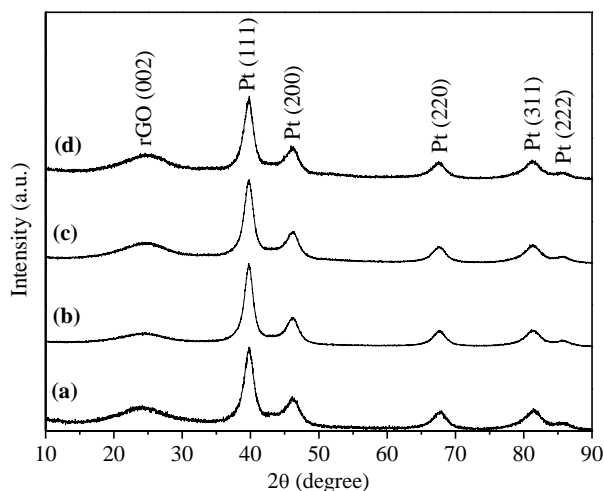


Figure 6. X-ray diffraction patterns of electrocatalysts supported on reduced graphene oxide: Pt (a), $\text{Pt}_{0.95}\text{Sn}_{0.05}$ (b), $\text{Pt}_{0.85}\text{Sn}_{0.15}$ (c) and $\text{Pt}_{0.75}\text{Sn}_{0.25}$ (d).

Table 1. Properties of Pt and Pt_xSn_y electrocatalysts supported on graphene-like films

Sample	Pt content (%) [*]		Sn content (%) [*]		Pt lattice parameter (nm) ^{**}	Pt crystallite size (nm) ^{***}	$\epsilon (\times 10^{-3})$ ^{***}
	wt	mol	wt	mol			
Pt	21.4 ⁺	–	–	–	3.9156	5.46	14.45
$\text{Pt}_{0.95}\text{Sn}_{0.05}$	19.3	94.4	0.7	5.6	3.9211	5.67	17.78
$\text{Pt}_{0.85}\text{Sn}_{0.15}$	18.2	86.1	1.8	13.9	3.9220	5.63	19.26
$\text{Pt}_{0.75}\text{Sn}_{0.25}$	16.4	73.5	3.6	26.5	3.9234	5.66	19.61

⁺Determined by TG analysis

^{*}Determined by EDX microanalysis

^{**}Determined by Rietveld analysis

^{***}Determined by Williamson-Hall analysis

Based on Williamson-Hall analysis, plots were drawn with $\sin(\theta)$ along the x -axis and $\beta_{(hkl)} \cdot \cos(\theta)$ along the y -axis for all electrocatalysts as shown in Fig. 7. From the linear fit of the data, the mean Pt crystallite size was estimated from the intercept and the micro-strain (ϵ) component from the slope of the plots. As summarized in Table 1, the results of mean crystallite size were in close agreement with TEM results. Moreover, the micro-strain component increased with Sn addition, which suggests an increasing lattice deformation stress as a consequence of the incorporation of greater amounts of Sn atoms.

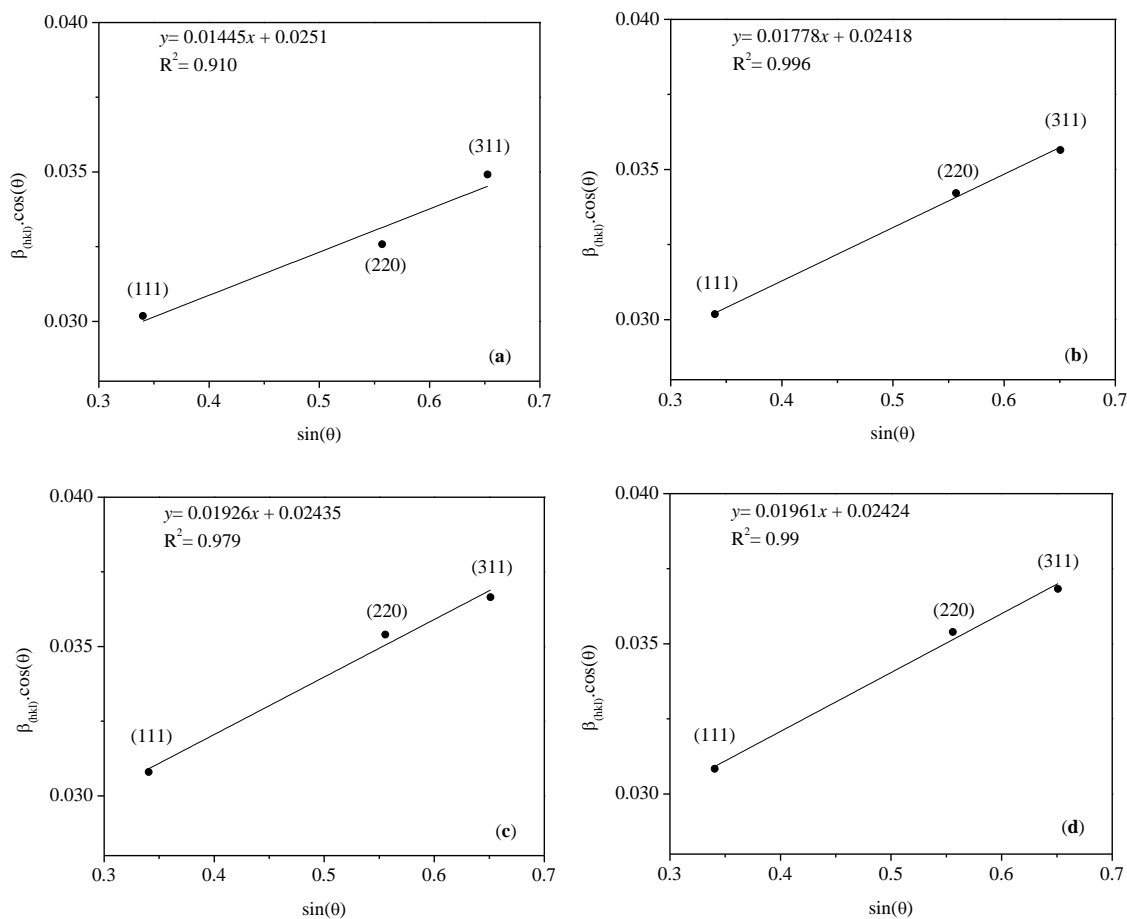


Figure 7. Williamson-Hall (W-H) plots of electrocatalysts supported on reduced graphene oxide: Pt (a), Pt_{0.95}Sn_{0.05} (b), Pt_{0.85}Sn_{0.15} (c) and Pt_{0.75}Sn_{0.25} (d). Each data point on the plots was labeled according to the index of its (hkl) reflections.

3.3. Electrochemical properties of Pt/rGO and Pt_xSn_y/rGO electrocatalysts

The process of electro-oxidation of Pt and Pt_xSn_y electrodes in 0.5 mol·L⁻¹ H₂SO₄ solutions is presented in Fig. 8. In relation to the forward scan, well-defined current peaks were observed in the potential range 0.05–0.3 V, corresponding to desorption of H₂ due to oxidation of adsorbed atomic hydrogen on Pt surface [35]. In general, the shape of these peaks is independent of Sn amount, indicating that the same Pt active sites are available for reactions. In relation to the commercial Pt catalyst (Pt/C), poor-defined current peaks were observed possibly due to a minor exposure of Pt sites for reaction. Broadened hydrogen desorption regions were presented by Pt_xSn_y catalysts cyclic voltammograms, confirming the effect of Sn atoms in the promotion of Pt activity. Despite the absence of Sn electro-activity [13] and the lower Pt amount, the results indicate that Pt_xSn_y catalysts were more effective towards hydrogen electro-oxidation. On the one hand, this effect can be explained by an electronic enrichment of Pt *d*-band due to incorporation of Sn atoms into Pt lattice, as demonstrated by Rietveld analysis (Table 1). Moreover, alloying contributed to an increasing lattice strain, according to Williamson-Hall analysis (Table 1), which probably led to the formation of several reactive defects.

A flat region ranging from 0.3 to 0.4 V was observed for Pt/rGO (Fig. 8). There is almost no current in this region, suggesting the absence of faradaic charge transfer reactions on the electrode. Nevertheless, the measured current results from non-faradaic processes, such as the accumulation of partially or fully solvated H^+ at Pt/electrolyte interface (double-layer region). After Sn addition, the overall behavior of the double-layer charging region is another indicative of the direct influence of Sn on changing the electronic population of d orbitals of the platinum atoms.

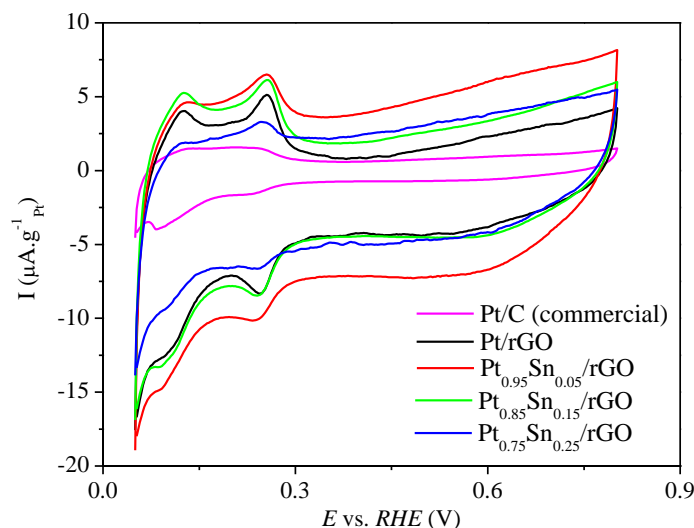


Figure 8. Cyclic voltammograms of N_2 -saturated $0.5 \text{ mol}\cdot\text{L}^{-1} \text{ H}_2\text{SO}_4$ solutions of studied electrocatalysts. The scan rate was $10 \text{ mV}\cdot\text{s}^{-1}$ and all potentials were referred to the reversible hydrogen electrode (RHE) at room temperature and atmospheric pressure.

As the electrode potential increased, a current gain was observed at about 0.4 V for Pt/rGO as a result of charge transfer due to the oxidation of water followed by formation of adsorbed atomic oxygen on Pt [35]. When compared to the commercial catalyst, Pt oxidation seems to occur at a lesser extent since carbon black possibly contains a minor concentration of oxygen functional groups than the synthesized graphene-like film. This result indicates that the presence of oxygen functional groups on reduced graphene oxide support strongly promotes the oxidation of Pt surface, in accordance with Sharma et al. [36]. In the case of Sn-containing catalysts, the promotional effect confirmed by the voltammograms might be due to an ability of the doped Pt phase to adsorb atomic oxygen from reactive oxygen species, such as OH^- or O^{2-} , originated from water oxidation. Beyond the onset of surface oxidation, further increase of the potential has been related to the formation of thin layers of Pt oxides onto which PtO_2 continues growing [35], the latter being attributed to the higher-potential range in Fig. 8 (0.6–0.8 V).

The results of ethanol electro-oxidation over Pt and Sn-containing Pt catalysts supported on reduced graphene oxide in $0.5 \text{ mol}\cdot\text{L}^{-1} \text{ H}_2\text{SO}_4/1.0 \text{ mol}\cdot\text{L}^{-1} \text{ C}_2\text{H}_5\text{OH}$ solutions are shown in Fig. 9.

From the results of cyclic voltammetry (Fig. 9), it is observed that EOR starts around 0.4 V at the electrode coated with Pt/C. In a general way, the use of an alternative carbon nanomaterial as support, in turn, shifted the forward scan curves to more negative potentials by around 0.1 V, demonstrating the efficiency of the synthesized graphene-like support.

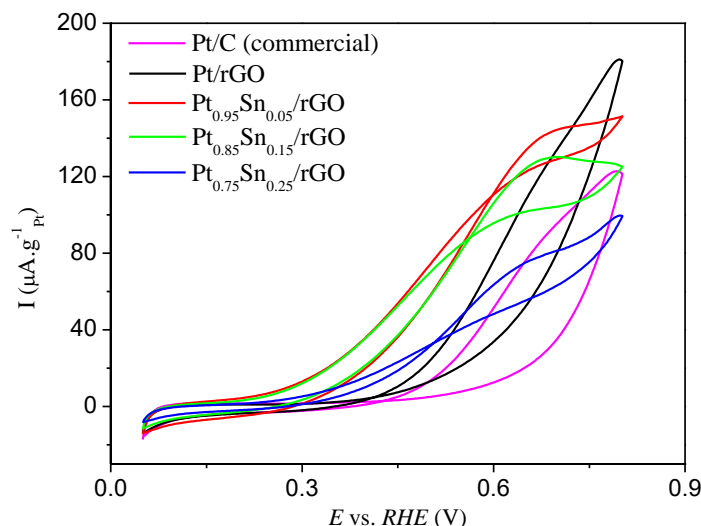


Figure 9. Cyclic voltammograms of N_2 -purged $0.5 \text{ mol}\cdot\text{L}^{-1} \text{ H}_2\text{SO}_4/1.0 \text{ mol}\cdot\text{L}^{-1} \text{ C}_2\text{H}_5\text{OH}$ solutions at several electrodes. The scan rate was $10 \text{ mV}\cdot\text{s}^{-1}$ and all potentials were referred to the reversible hydrogen electrode (RHE) at room temperature and atmospheric pressure.

The results of EOR are indicative of the capability of reduced graphene oxide to transfer oxygenated species to Pt nanoparticles, thus improving the catalyst ability to oxidize strongly adsorbed intermediates. As a consequence, the onset potential is lowered since more sites are available for reaction. The addition of Sn also shifted the forward scan curves to even more negative potentials by around 0.2 V (Fig. 9). $\text{Pt}_x\text{Sn}_y/\text{rGO}$ were more active for EOR. This effect could be attributed to both bifunctional mechanism and electronic effect. In relation to the former, Sn and/or rGO provided oxygen species for the oxidation of the adsorbed intermediates. The latter was associated to an electronic enrichment of Pt d orbital due to alloying [8, 37-39].

Chronoamperometry measurements were carried out at 0.5 V for 30 min over all electrodes in $0.5 \text{ mol}\cdot\text{L}^{-1} \text{ H}_2\text{SO}_4/1.0 \text{ mol}\cdot\text{L}^{-1} \text{ C}_2\text{H}_5\text{OH}$ solutions, and the results are presented in Fig. 10.

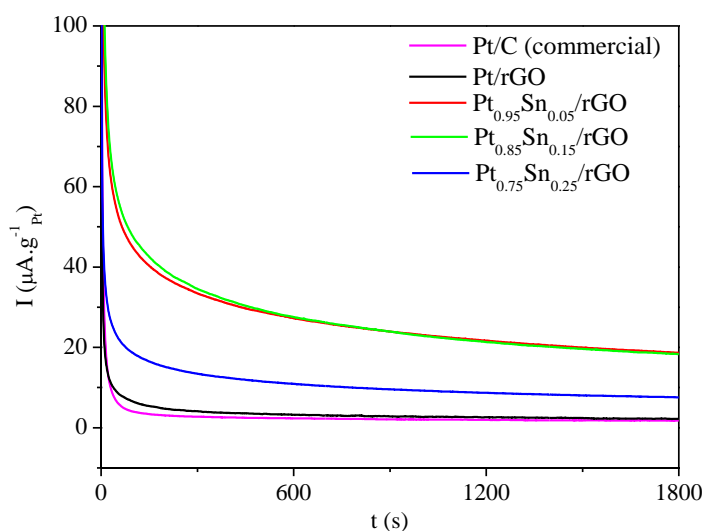


Figure 10. Chronoamperometric curves of ethanol oxidation at several electrodes in N_2 -purged $0.5 \text{ mol}\cdot\text{L}^{-1} \text{ H}_2\text{SO}_4/1.0 \text{ mol}\cdot\text{L}^{-1} \text{ C}_2\text{H}_5\text{OH}$ solutions. All measurements were carried out under a constant applied potential of 0.5 V at room temperature and atmospheric pressure.

A sharp decrease in current was observed in the first seconds for Pt/C and Pt/rGO, which can be attributed to the presence of strongly adsorbed intermediates (Fig. 10). The current values at the end of the measurements were summarized in Table 2. According to these data, Pt presented a higher activity towards EOR when supported on rGO.

Chronoamperometry measurements on PtSn catalysts revealed a major poison-preventing effect of the promoter, which led to an enhanced catalytic activity (Fig. 10). A comparative analysis among the behavior of Pt_xSn_y catalysts (Fig. 10) suggests that the addition of 5–15 mol % Sn might impact better on Pt activity. Presented results suggest that higher doping concentration decreases catalyst activity. The difference of activity is attributed to different grade of interaction between Pt and Sn in bimetallic catalysts [40].

Table 2. Comparison of chronoamperometry results

Catalyst composition	Current ($\mu\text{A}\cdot\text{g}^{-1}_{\text{Pt}}$)
	After 1800 s
Pt/C	1.8
Pt/rGO	2.3
$Pt_{0.95}Sn_{0.05}/\text{rGO}$	18.7
$Pt_{0.85}Sn_{0.15}/\text{rGO}$	18.3
$Pt_{0.75}Sn_{0.25}/\text{rGO}$	7.6

The electrochemical characteristics of representative graphene-based PtSn catalysts are summarized in Table 3.

Table 3. Electrochemical characteristics of graphene-based PtSn catalysts

Materials	Current density ($\text{mA}\cdot\text{cm}^{-2}$)	Onset potential (V)	Remark	Ref.
Pt_3Sn/GO	~ 30	–	EOR	[13]
$Pt/\text{SnO}_2/\text{G}$	$\sim 100 \text{ A}\cdot\text{g}^{-1}_{\text{Pt}}$ at 0.6 V vs. Ag/AgCl	0.31 vs. Ag/AgCl	EOR	[14]
$\text{SnO}_2/\text{Pt}/\text{G}_{30}$	$\sim 18 \text{ mA}\cdot\text{mg}^{-1}_{\text{Pt}}$ at –0.15 V vs. Hg/Hg ₂ SO ₄	–0.045 vs. Hg/Hg ₂ SO ₄	EOR	[41]
$\text{Pt-Sn}(95:5)/\text{G}$	$131.2 \text{ mA}\cdot\text{mg}^{-1}_{\text{Pt}}$ at 0.65 V vs. SCE	–	EOR	[42]

A study on the ethanol oxidation over Pt_3Sn/GO in acidic medium was carried out by Kakei [13]. According to the chronoamperometric studies, the EOR activity of graphene oxide supported Pt_3Sn was increased about 3 times compared with graphene oxide supported Pt. This result demonstrated that the addition of Sn could reduce CO and carbonaceous species poisoning and enhance Pt activity. A similar trend was observed in our study. Particularly, $Pt_{0.95}Sn_{0.05}/\text{graphene}$ ($0.4935 \text{ mA}\cdot\text{cm}^{-2}$ at 0.5 V vs. RHE) showed a ~ 8.5 times higher current density than that of our Pt/graphene ($0.0584 \text{ mA}\cdot\text{cm}^{-2}$ at 0.5 V vs. RHE).

Other similar work by Qu et al. [14] demonstrated that Pt/SnO₂/graphene composites exhibited about 2 times higher electrocatalytic activity than Pt/graphene at 0.6 V vs. Ag/AgCl. The onset potential of Pt/SnO₂/graphene for EOR in acidic medium was 0.31 V vs. Ag/AgCl, which was lower than that of Pt/graphene (0.46 V vs. Ag/AgCl). Authors attributed the enhanced activity to the close-connected structure between Pt and SnO₂ nanoparticles, which led to earlier electro-oxidation of poisonous intermediates. The unique properties of PtSn catalysts for EOR were also observed in our study. Specifically, the onset potential of Pt_{0.95}Sn_{0.05} and Pt_{0.85}Sn_{0.15} was in the range 0.175–0.30 V vs. RHE whereas the onset potential of Pt/graphene was around 0.30–0.45 V vs. RHE. Differently from Qu et al. [14], we attributed the enhanced activity for EOR to both bifunctional mechanism and electronic effect. In relation to the former, Sn and/or rGO provided oxygen species for the oxidation of the poisonous species while the latter was associated to an electronic enrichment of Pt *d* orbital due to alloying.

Some other PtSn catalysts also improved ethanol electro-oxidation. Qu et al. [41] demonstrated the synthesis of layer-by-layer SnO₂ nanosheet/Pt/graphene via microwave method. The layer-by-layer composite exhibited about 3 times higher specific current in acidic medium than bare Pt/graphene. Wang et al. [42] also prepared PtSn alloys on graphene sheets via chemical reduction of graphene oxide, H₂PtCl₆ and SnCl₂ using a polyalcohol method. Chronoamperometry results revealed that addition of 5 wt% Sn was the most efficient in enhancing Pt activity. The Pt-Sn(95:5)/graphene catalyst exhibited about 1.1 time higher specific current in acidic medium than Pt-Sn(100:0)/graphene.

In comparison to the results found in cited works, the enhanced electrocatalytic activity of our catalysts may be attributed to the incorporation of Sn atoms into Pt lattice, as demonstrated by XRD results (Table 1 and Figure 7). In this way, alloying can significantly influence Pt *d* orbital thus maximizing for efficient electron transfer.

3.4. Single direct ethanol fuel cell (DEFC) performance

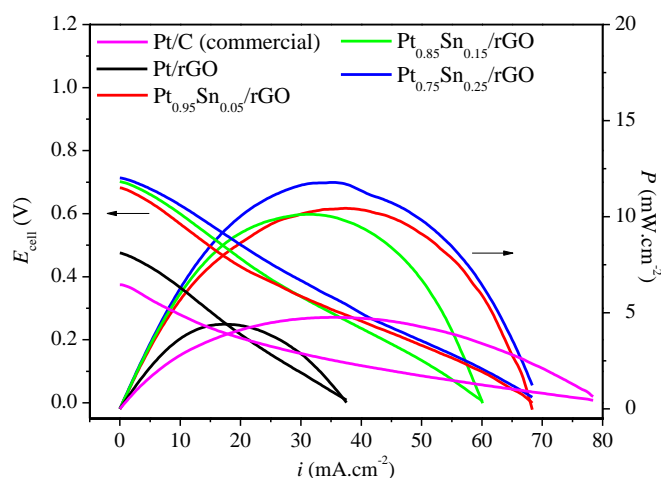


Figure 11. Electric characteristics of single 5 cm² DEFC with reduced graphene oxide-supported 20 wt% Pt and Pt_xSn_y as anode catalysts, Nafion 117 as electrolyte and carbon-supported 20 wt% Pt (BASF) as cathode catalysts. A 1.0 mg·cm⁻² Pt loading was used to fabricate all electrodes. Fuel cell tests were carried out at 100 °C. Ethanol (2.0 mol·L⁻¹) was fed in the anode at 1.0 mL·min⁻¹ under 1.0 bar pressure and pure humidified oxygen was fed in the cathode at 200 sccm under 2.0 bar pressure.

The electric characteristics of single DEFCs with Pt/rGO and Pt_xSn_y/rGO as anode catalysts and Pt/C as cathode catalysts are presented in Fig. 11. The results of polarization measurements pointed that ethanol oxidation is a much slower reaction over Pt/C, which was indicated by the highest overpotential. A decrease in overpotential value was observed for Pt/rGO anode catalyst. The increase in open circuit voltage can be explained by a decrease in Pt surface poisoning due to the ability of the catalytic surface to promote the oxidation of the strongly adsorbed reaction intermediates. In relation to Pt_xSn_y anode catalysts, overpotential decreased significantly as a result of Pt electronic enrichment due to Sn atoms dissolution.

All gas diffusion anodes containing graphene-like supports presented strong ohmic limitations (Fig. 11). This feature might be associated to the presence of oxygen functional groups on rGO nanosheets (Fig. 2), which decreased support electronic mobility, as well as to the restacking of the sheets during MEAs fabrication, which compromised Pt accessible surface area [43-45]. The difference in ohmic polarization region between Pt and Pt_xSn_y may be correlated to an enriched surface charge density on Sn-promoted electrodes.

Moreover, the polarization curves (Fig. 11) did not point to mass transport limitations at high current densities for both Pt/rGO and Pt_xSn_y/rGO catalysts. Therefore, it seems that the rate of ethanol molecules diffusion over the support is, at least, comparable to the rate of conversion to products, which means that the reaction is not diffusion-limited. In contrast to the effect reported by Marinkas et al. [46], the reduced graphene oxide synthesized in the present work may be a suitable support for controlling the transport of both reagents and products, feature that might be related to the presence of oxygen-containing functional groups (Fig. 2). A summary of the electric characteristics of single DEFCs is presented in Table 4.

Table 4. Characteristics of DEFCs, at 100 °C, with commercial Pt/C and synthesized Pt and Pt_xSn_y anode catalysts supported on reduced graphene oxide

Anode composition	Open circuit voltage (mV)	η^* (mV)	$P_{\max.}$ (mW·cm ⁻²)	i^{**} (mA·cm ⁻²)
Pt/C	374.4	769.6	4.7	35.4
Pt/rGO	475.3	668.7	4.4	17.4
Pt _{0.95} Sn _{0.05} /rGO	682.2	461.8	10.4	37.2
Pt _{0.85} Sn _{0.15} /rGO	701.5	442.5	10.1	31.7
Pt _{0.75} Sn _{0.25} /rGO	713.4	430.6	11.8	35.4

*The overpotential (η) was calculated as the difference between the theoretical potential (1.144 V) and the open circuit voltage.

**Current density measured at maximum power density.

In a general way, the bimetallic Pt_xSn_y system led to an enhancement of EOR followed by an improvement in cell electric performance. Interestingly, single fuel cell tests revealed that Pt_{0.75}Sn_{0.25} was the most efficient anode catalyst in contrast to electrochemical measurements data. As the same Pt loading was used in the fabrication of all membrane/electrodes assemblies, differences in anodic

performance are probably related to the structural properties of Pt nanoparticles. Finally, the hypothetical mechanism of ethanol oxidation may be mediated by a combination of both electronic and bifunctional effects. The former is mainly related to Pt electronic enrichment and the presence of reactive defects due to Sn atoms dissolution, which enhanced catalyst activity. The latter is based on the presence of abundant oxygen functional groups on the surfaces of reduced graphene oxide nanosheets, which potentially depressed poisoning by reaction intermediate products.

4. CONCLUSIONS

Oxidation-exfoliation of graphite followed by reduction with L-ascorbic acid demonstrated to be a suitable method for the synthesis of reduced graphene oxide. After deposition of Pt and Sn by an impregnation–reduction method, resultant reduced graphene oxide composite catalysts were constituted by PtSn in separate phase from the graphene-like film. Sn loading strongly affected physical and chemical properties of composite powders. In relation to the performance of the designed nanomaterials for EOR, the presence of Sn had a major impact on promoting Pt electrocatalytic activity, which was strongly influenced by the addition of Sn in an alloyed form, while rGO mainly helped in the oxidation of the strong adsorbed intermediates. In summary, PtSn exhibited lower oxidation potentials and higher current densities for EOR. A further work is necessary to investigate the reaction pathway of ethanol oxidation over these electrocatalysts.

ACKNOWLEDGMENTS

Authors would like to thank National Council for Scientific and Technological Development (CNPq, Brazil) for financial support and the members from the following laboratories: X-ray Diffraction (CCTM/IPEN), Microscopy and Microanalysis (CCTM/IPEN), Thermal Analysis (CCCH/IPEN) and Vibrational Spectroscopy (IQ/USP).

References

1. A. Brouzgou, A. Podias and P. Tsiakaras, *J Appl Electrochem*, 43 (2013) 119.
2. D. Pottmaier, C. R. Melo, M. N. Sartor, S. Kuester, T. M. Amadio, C. A. H. Fernandes, D. Marinha and O. E. Alarcon, *Renew Sust Energ Rev*, 19 (2013) 678.
3. N. M. Julkapli and S. Bagheri, *Int J Hydrogen Energ*, 40 (2015) 948.
4. S. Sharma and B. G. Pollet, *J Power Sources*, 208 (2012) 96.
5. G. A. Camara, R. B. de Lima and T. Iwasita, *Electrochem Commun*, 6 (2004) 812.
6. A. O. Neto, M. J. Giz, J. Perez, E. A. Ticianelli and E. R. Gonzalez, *J Electrochem Soc*, 149 (2002) A272.
7. W. J. Zhou, S. Q. Song, W. Z. Li, Z. H. Zhou, G. Q. Sun, Q. Xin, S. Douvartzides and P. Tsiakaras, *J Power Sources*, 140 (2005) 50.
8. F. E. López-Suárez, C. T. Carvalho-Filho, A. Bueno-López, J. Arboleda, A. Echavarría, K. I. B. Eguiluz and G. R. Salazar-Banda, *Int J Hydrogen Energ*, 40 (2015) 12674.
9. E. Antolini and E. R. Gonzalez, *J Power Sources*, 195 (2010) 3431.
10. M. Z. F. Kamarudin, S. K. Kamarudin, M. S. Masdar and W. R. W. Daud, *Int J Hydrogen Energ*, 38 (2013) 9438.

11. K. S. Novoselov, A. K. Geim, S. V. Morosov, D. Jiang, Y. Zhang, S. V. Dubonos, I. V. Grigorieva and A. A. Firsov, *Science*, 306 (2004) 666.
12. E. P. Randviir, D. A. C. Brownson and C. E. Banks, *Mater Today*, 17 (2015) 426.
13. K. Kakaei, *Electrochim Acta*, 65 (2015) 330.
14. Y. Qu, Y. Gao, L. Wang, J. Rao and G. Yin, *Chem Eur J*, 22 (2016) 193.
15. K. E. W. Jr and P. E. Sheehan, *Diam Relat Mater*, 46 (2014) 25.
16. B. C. Brodie, *Phil Trans R Soc*, 149 (1859) 249.
17. L. Staudenmaier, *Ber Dtsch Chem Ges* 31 (1898) 1481.
18. W. S. Hummers and R. E. Offeman, *J Am Chem Soc*, 80 (1958) 1339.
19. D. C. Marcano, D. V. Kosynkin, J. M. Berlin, A. Sinitskii, Z. Sun, A. Slesarev, L. B. Alemany, W. Lu and J. M. Tour, *Acs Nano*, 4 (2010) 4806.
20. A. Martín and A. Escarpa, *Trend Anal Chem*, 56 (2014) 13.
21. C. K. Chua and M. Pumera, *Chem Soc Rev*, 43 (2014) 291.
22. J. Zhang, H. Yang, G. Shen, P. Cheng, J. Zhang and S. Guo, *Chem Commun*, 46 (2010) 1112.
23. D. He, L. Shen, X. Zhang, Y. Wang, N. Bao and H. H. Kung, *AIChE J*, 60 (2014) 2757.
24. S. Abdolhosseinzadeh, H. Asgharzadeh and H. S. Kim, *Nature*, 5 (2015) 1.
25. M. I. Bowman, *J Chem Educ*, 26 (1949) 103.
26. T. J. Schmidt, H. A. Gasteiger, G. D. Stäb, P. M. Urban, D. M. Kolb and R. J. Behm, *J Electrochem Soc*, 145 (1998) 2354.
27. C. Botas, P. Álvarez, P. Blanco, M. Granda, C. Blanco, R. Santamaría, L. J. Romasanta, R. Verdejo, M. A. López-Manchado and R. Menéndez, *Carbon*, 65 (2013) 156.
28. S. You, S. M. Luzan, T. Szabó and A. V. Talyzin, *Carbon*, 52 (2013) 171.
29. I. K. Moon, J. Lee, R. S. Ruoff and H. Lee, *Nat Commun*, 1 (2010) 1.
30. Y. Hu, S. Song and A. Lopez-Valdivieso, *J Colloid Interface Sci*, 450 (2015) 68.
31. F. Pendolino, G. Capurso, A. Maddalena and S. L. Russo, *RSC Adv*, 4 (2014) 32914.
32. L. Stobinski, B. Lesiak, A. Malolepszy, M. Mazurkiewicz, B. Mierzwa, J. Zemek, P. Jiricek and I. Bieloshapka, *J Electron Spectrosc Relat Phenom*, 195 (2014) 145.
33. M. S. Dresselhaus, A. Jorio, M. Hofmann, G. Dresselhaus and R. Saito, *Nano Lett*, 10 (2010) 751.
34. M. S. Dresselhaus, A. Jorio and R. Saito, *Annu Rev Condens Matter Phys*, 1 (2010) 89.
35. T. Jacob, *Fuel cell catalysis: A surface science approach*, John Wiley & Sons, Inc., (2009) New Jersey, US.
36. S. Sharma, A. Ganguly, P. Papakonstantinou, X. Miao, M. Li, J. L. Hutchison, M. Delichatsios and S. Ukleja, *J Phys Chem C*, 114 (2010) 19459.
37. M. T. M. Koper, S. C. S. Lai and E. Herrero, *Fuel cell catalysis: A surface science approach*, John Wiley & Sons, Inc., (2009) New Jersey, US.
38. F. Han, X. Wang, J. Lian and Y. Wang, *Carbon*, 50 (2012) 5498.
39. R. Crisafulli, R. M. Antoniassi, A. O. Neto and E. V. Spinacé, *Int J Hydrogen Energ*, 39 (2014) 5671.
40. F. Colmati, E. Antolini and E. R. Gonzalez, *Electrochim Acta*, 50 (2005) 5496.
41. Y. Qu, C. Li, L. Wang, Y. Gao, J. Rao and G. Yin, *Int J Hydrogen Energ*, 41 (2016) 14036.
42. Y. Wang, G. Wu, Y. Wang and X. Wang, *Electrochim Acta*, 130 (2014) 135.
43. J. Y. Park and S. Kim, *Int J Hydrogen Energ*, 38 (2013) 6275.
44. J. Luo, J. Kim and J. Huang, *Acc Chem Res*, 46 (2013) 2225.
45. B. Luo, X. Yan, S. Xu and Q. Xue, *Int J Hydrogen Energ*, 59 (2012) 429.
46. A. Marinkas, F. Arena, J. Mitzel, G. M. Prinz, A. Heinzl, V. Peinecke and H. Natter, *Carbon*, 58 (2013) 139.